Cellular/Molecular

Disruption of the Presynaptic Cytomatrix Protein Bassoon Degrades Ribbon Anchorage, Multiquantal Release, and Sound Encoding at the Hair Cell Afferent Synapse

Zhizi Jing,[1] Mark A. Rutherford,[2]* Hideki Takago,[2,3,4]* Thomas Frank,[2] Anna Fejtova,[5] Darina Khimich,[2] Tobias Moser,[2,3,6] and Nicola Strenzke[1]

[1]Auditory Systems Physiology Group, InnerEarLab, and [2]InnerEarLab, Department of Otolaryngology and Collaborative Research Center 889, University Medical Center, 37075 Göttingen, Germany, [3]Bernstein Focus for Neurotechnology, University of Göttingen, 37075 Göttingen, Germany, [4]Department of Rehabilitation for Sensory Functions, Research Institute, National Rehabilitation Center for Persons with Disabilities, Saitama 359-8555, Japan, [5]Leibniz Institute for Neurobiology, 39118 Magdeburg, Germany, and [6]Center for Nanoscopy and Molecular Physiology of the Brain, University of Göttingen, 37075 Göttingen, Germany

Inner hair cells (IHCs) of the cochlea use ribbon synapses to transmit auditory information faithfully to spiral ganglion neurons (SGNs). In the present study, we used genetic disruption of the presynaptic scaffold protein bassoon in mice to manipulate the morphology and function of the IHC synapse. Although partial-deletion mutants lacking functional bassoon (Bsn$^{\Delta Ex4/5}$) had a near-complete loss of ribbons from the synapses (up to 88% ribbonless synapses), gene-trap mutants (Bsn^{gt}) showed weak residual expression of bassoon and 56% ribbonless synapses, whereas the remaining 44% had a loosely anchored ribbon. Patch-clamp recordings and synaptic Ca$_V$1.3 immunolabeling indicated a larger number of Ca^{2+} channels for Bsn^{gt} IHCs compared with Bsn$^{\Delta Ex4/5}$ IHCs and for Bsn^{gt} ribbon-occupied versus Bsn^{gt} ribbonless synapses. An intermediate phenotype of Bsn^{gt} IHCs was also found by membrane capacitance measurements for sustained exocytosis, but not for the size of the readily releasable vesicle pool. The frequency and amplitude of EPSCs were reduced in Bsn$^{\Delta Ex4/5}$ mouse SGNs, whereas their postsynaptic AMPA receptor clusters were largely unaltered. Sound coding in SGN, assessed by recordings of single auditory nerve fibers and their population responses *in vivo*, was similarly affected in Bsn^{gt} and Bsn$^{\Delta Ex4/5}$ mice. Both genotypes showed impaired sound onset coding and reduced evoked and spontaneous spike rates. In summary, reduced bassoon expression or complete lack of full-length bassoon impaired sound encoding to a similar extent, which is consistent with the comparable reduction of the readily releasable vesicle pool. This suggests that the remaining loosely anchored ribbons in Bsn^{gt} IHCs were functionally inadequate or that ribbon independent mechanisms dominated the coding deficit.

Introduction

Sensory hair cells, electroreceptors, retinal photoreceptors, and bipolar cells use a specialized synaptic machinery for fast and indefatigable sustained neurotransmitter release to encode transient and prolonged sensory stimuli precisely. Their morphological hallmark is the synaptic ribbon, an electron-dense structure tethering a halo of synaptic vesicles (tom Dieck and Brandstätter, 2006; for review, see Nouvian et al., 2006; Schmitz, 2009; Matthews and Fuchs, 2010; Rutherford and Pangršič, 2012). Several experimental approaches have indicated the functional importance of the ribbon, including biochemical studies of its major component, RIBEYE (Schwarz et al., 2011), genetic manipulation (Dick et al., 2003; Khimich et al., 2005; Sheets et al., 2011), studies of physiological ribbon dynamics (Remé and Young, 1977; Spiwoks-Becker et al., 2004; Hull et al., 2006; Emran et al., 2010), and acute photodamage (Snellman et al., 2011). Based on such data, two major functions of the ribbon can be hypothesized: (1) establishing and stabilizing a large number of vesicular release sites and Ca^{2+} channels at the active zone, i.e., a large readily releasable vesicle pool (RRP; Khimich et al., 2005; Hull et al., 2006; Frank et al., 2010) and (2) rapid refilling of the RRP of synaptic vesicles (von Gersdorff et al., 1996; LoGiudice et al., 2008; Frank et al., 2010; Snellman et al., 2011). A third emerging hypothesis suggests a role of the ribbon in synchronous multi-

quantal release (MQR; (Heidelberger et al., 1994; Parsons and Sterling, 2003; Edmonds, 2004; Fuchs, 2005; Matthews and Sterling, 2008; Graydon et al., 2011). MQR has been reported for inner ear and retinal ribbon synapses (Glowatzki and Fuchs, 2002; Singer et al., 2004; Neef et al., 2007; Li et al., 2009).

The large 420 kDa scaffold protein bassoon interacts with RIBEYE (tom Dieck et al., 2005) and thereby contributes to the anchorage of the ribbon to the active zone of photoreceptors (Dick et al., 2003) and inner hair cells (IHCs) (Khimich et al., 2005). By promoting a high abundance of Ca^{2+} channels and release sites for readily releasable vesicles (Khimich et al., 2005; Frank et al., 2010), bassoon and/or the ribbon enable high rates of spiral ganglion neuron (SGN) firing (Buran et al., 2010; Frank et al., 2010). In the present study, we show that a higher fraction of preserved synaptic ribbons in bassoon gene-trap IHCs (Frank et al., 2010; Hallermann et al., 2010; Bsn^{gt}) is associated with a weaker IHC phenotype compared with mostly ribbonless $Bsn^{\Delta Ex4/5}$ IHCs (mice with deletion of exons 4 and 5 of the *bassoon* gene (Altrock et al., 2003; Khimich et al., 2005) in terms of Ca^{2+} currents, and sustained exocytosis, whereas RRP size in Bsn^{gt} IHCs and sound encoding in Bsn^{gt} SGNs are not improved. Using immunofluorescence microscopy, we found a greater distance of the ribbon from the active zone in Bsn^{gt} IHCs and propose that those loosely anchored ribbons are not fully functional. Finally, using patch-clamp recordings from postsynaptic SGN boutons of $Bsn^{\Delta Ex4/5}$ mice, we found a normal range of EPSC amplitudes but lower mean amplitudes and rates, suggesting that the ribbon is not essential but is supportive for MQR.

Materials and Methods

Animals. Mice of either sex with a targeted deletion of exons 4 and 5 of the *bassoon* gene ($Bsn^{\Delta Ex4/5}$; Altrock et al., 2003) or *bassoon* gene-trap mutants (Frank et al., 2010; Hallermann et al., 2010; Bsn^{gt}; derived from Omnibank ES cell line OST486029; Lexicon Pharmaceuticals) and their respective heterozygous ($Hz_{\Delta Ex4/5}$) and wild-type littermates ($WT_{\Delta Ex4/5}$ and WT_{gt}) were used for experiments. The genetic background for the $Bsn^{\Delta Ex4/5}$ animals is characterized as C57BL/6 × 129Sv. For Bsn^{gt} mice, it is an uncharacterized background derived from the same strains. All experiments complied with national animal care guidelines and were approved by the University of Göttingen Board for animal welfare and the animal welfare office of the state of Lower Saxony.

Immunohistochemistry and confocal microscopy. The cochlea was opened near the apex and fixed in 99% methanol for 20 min at $-20°C$. Apical half-turns of organs of Corti were carefully explanted and immunostaining of the whole mounts was performed as described previously (Khimich et al., 2005, Meyer et al., 2009; Frank et al., 2010), but using donkey serum (Genetex) instead of goat serum buffer for blocking and dilution of antibodies. The following antibodies were used: goat anti-CtBP2 (1:150; Santa Cruz Biotechnology), mouse anti-GluA2 (1:75; Millipore), rabbit anti-$Ca_V1.3$ (1:75; Alomone Labs), mouse anti-bassoon SAP7F407 (Abcam), and secondary Alexa Fluor 488-conjugated anti-mouse, Alexa Fluor 596-conjugated anti-goat, and Alexa Fluor 647-conjugated anti-rabbit IgG antibodies (1:200, Invitrogen). Confocal morphological images were acquired using a laser scanning confocal microscope (SP5; Leica) with 100× oil-immersion objectives, avoiding the extreme apical regions. In each experiment, organs of Corti of mutant and WT animals 29–75 d of age were processed in parallel using identical staining, mounting, laser excitation power, and microscope emission and detection settings. Experiments were repeated until successful; preparations were judged successful if all antigens were labeled with relative uniformity in both genotypes on the same experiment. Each preparation yielded several images, each containing a row of 6 IHCs. Image stacks of synaptic regions selected for semiquantitative analysis were acquired at similar depths in the z-axis to control for attenuation. Preparations were discarded if bleaching was rapid or nonuniform across channels. The following numbers of pairs of successful preparations of both ears from

pairs of mutant/WT mice were included in the analysis: 3 GluA2/CtBP2/$Ca_V1.3$, 2 CtBP2/$Ca_V1.3$/bassoon, 1 $Ca_V1.3$/bassoon, and 2 GluA2/CtBP2. Stimulated emission depletion microscopy was performed with a custom microscope as in Frank et al. (2010).

The locations of synapses in confocal image stacks were defined as the centers of mass of fluorescent spots after thresholding by a subjective intensity criterion for each channel. The background (defined as the average voxel intensity in the entire synaptic region excluding voxels that exceeded the threshold value) was subtracted. Gaussian functions were fitted in all three dimensions to determine the center of mass of each cluster and the distance to the centers of mass of the nearest neighboring clusters in the other two channels within a 500 nm range. Immunofluorescence intensity was measured as the integral of the voxel values within a defined region of interest ($9 \times 9 \times 7$ voxels in the X, Y, and Z direction, which has the volume of $\sim 0.5 \times 0.5 \times 3.0\ \mu m$) centered on the voxel where the center of mass of each GluA2-positive cluster located.

Real-time PCR. Total RNA was isolated from preparations of the organ of Corti of 5-week-old mice using TRIzol reagent (Invitrogen). After reverse transcription with random hexamers, cDNA was subjected to real-time PCR using an ABI Prism 7900 Sequence Detection System (Applied Biosystems). cDNAs for Bsn, otoferlin, and TBP (TATA-binding protein as a housekeeping gene) were selectively amplified using the commercially available TaqMan Gene Expression Assays Mm01330351_mH, Mm00453306_m1, and Mm00446973_m1, respectively (Applied Biosystems) in separate reactions (20 μl volume) according to the manufacturer's protocol. Relative amounts of bassoon mRNAs, normalized to that of otoferlin, were calculated using the comparative $2^{-\Delta\Delta Ct}$ method (Applied Biosystems).

Patch-clamp of IHCs and postsynaptic boutons of SGNs. EPC-9 or EPC-10 amplifiers controlled by Patchmaster (HEKA Elektronik) were used for measurements. All voltages were corrected for liquid-junction potentials. IHCs from apical coils of freshly dissected organs of Corti (postnatal d 22–32) were patch-clamped as described previously (Moser and Beutner, 2000). The pipette solution for perforated-patch recordings contained the following (in mM): 120 Cs-glutamate (CsGlu), 13 tetraethylammonium (TEA)-Cl, 8 CsCl, 20 CsOH-HEPES, 1 $MgCl_2$, and 250 μg/ml amphotericin B (Calbiochem), pH 7.2. The pipette solution for whole-cell recordings contained the following (in mM): 100 CsGlu, 13 TEA-Cl, 8 CsCl, 20 CsOH-HEPES, 1 $MgCl_2$, 2 Mg-ATP, 0.3 Na-GTP, 5 EGTA, 1.5 $CaCl_2$, and 10 phosphocreatine disodium salt, pH 7.2. The extracellular solution contained the following (in mM): 95 NaCl, 35 TEA-Cl, 2.8 KCl, 10 $CaCl_2$, 1 $MgCl_2$, 1 CsCl, 10 NaOH-HEPES, and 10 D-glucose, pH 7.3. Currents were low-pass filtered at 5 kHz and sampled at 40 kHz. IHCs that showed a holding current exceeding -50 pA were discarded from analysis. Ca^{2+} currents were further isolated using a P/n protocol. For perforated-patch experiments, series resistance was required to be <30 MΩ. Membrane capacitance increments (ΔC_m) were measured as described previously (Moser and Beutner, 2000), averaging 100 ms before and 200 ms after (skipping the first 30 ms) the depolarization. We used 20 or 100 ms depolarizations and three interpulse intervals (98, 198, 398 ms) for dual-pulse experiments. For estimation of ΔC_{m1}, we averaged the membrane capacitance during the interpulse interval (C_{m1}) starting 30 ms after the end of the depolarization, and subtracted the baseline capacitance (averaged >100 ms before depolarization onset). Therefore, depending on the interpulse interval, the averaging window was 68, 168, and 368 ms long, respectively. For estimation of ΔC_{m2}, we averaged the membrane capacitance >200 ms (starting 30 ms after the second depolarization) and subtracted C_{m1}.

For display, ΔC_m traces (recorded at 1 kHz) were low-pass filtered at 50 Hz. Interstimulus periods were 2–3 s between Ca^{2+} current sweeps and 30–70 s for exocytosis measurements. Whole-cell recordings from postsynaptic boutons of 9- to 11-d-old SGNs were performed essentially as described previously (Glowatzki and Fuchs, 2002) using pipettes with small tip openings and resistance of 8–15 MΩ after pressure polishing (Goodman and Lockery, 2000). The pipette solution contained the following (in mM): 150 CsCl, 3.5 $MgCl_2$, 0.1 $CaCl_2$, 5 EGTA, 5 HEPES, and 2.5 Na_2ATP, pH 7.2. The extracellular solution contained the following (in mM): 5.8 KCl, 155 NaCl, 0.9 $MgCl_2$, 1.3 $CaCl_2$, 0.7 NaH_2PO_4, 5.6 D-glucose, and 10 HEPES, pH 7.4. In most recordings, tetrodotoxin (1–2
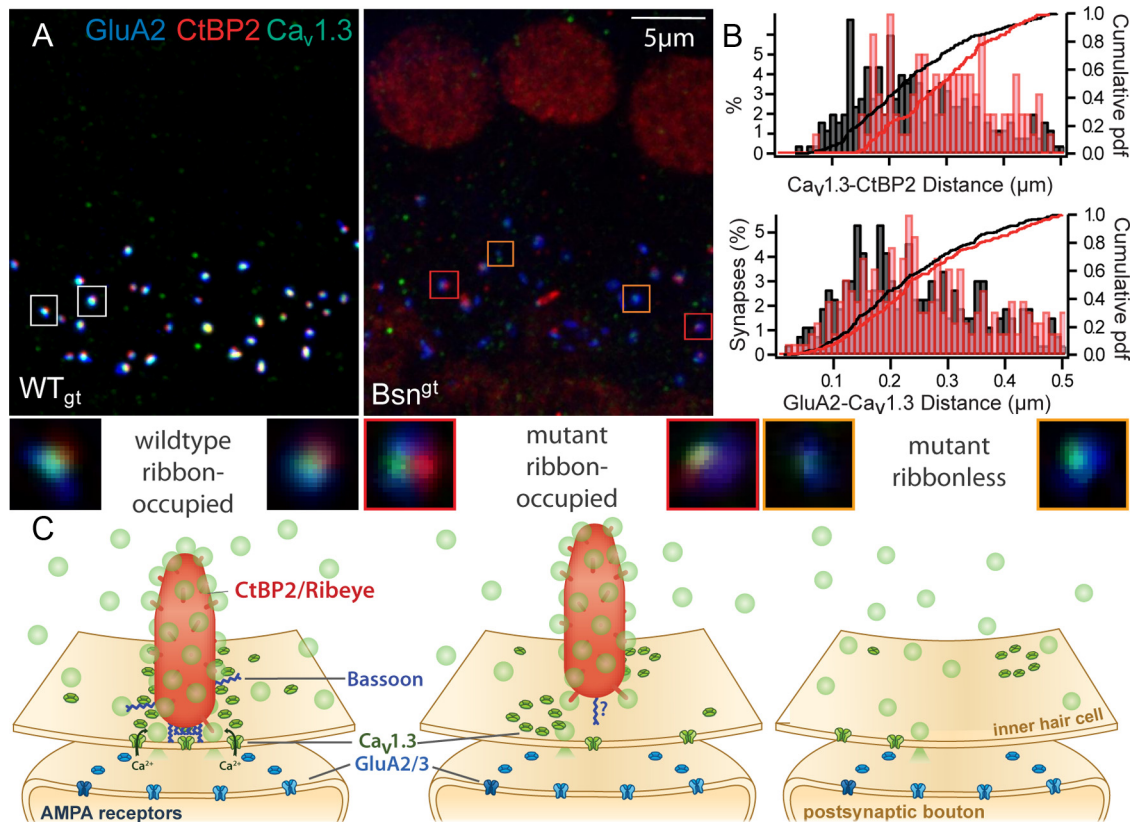
Figure 1. Bassoon contributes to anchoring the ribbon at the presynaptic membrane. ***A***, Rows of IHCs from a WT$_{gt}$ (left) and a Bsn ^{gt} mutant (right) mouse immunostained with antibodies against CtBP2 (red, labeling synaptic ribbons and nuclei), Ca$_V$1.3 (green, labeling presynaptic calcium channels), and GluA2 (blue, labeling postsynaptic glutamate receptors), illustrating a normal number of synapses but reduced ribbon occupancy in Bsn ^{gt} IHCs. ***B***, Distances between the centers of mass of CtBP2- and Ca$_V$1.3-immunoreactive clusters (top) at Bsn ^{gt} IHC synapses (red) were never as short as the closest ones in WT$_{gt}$ (black), suggesting disturbed ribbon anchorage to the presynaptic membrane. In contrast, the distance between Ca$_V$1.3 and GluA2-positive clusters (bottom) was comparable (from one representative pair of preparations). ***C***, Schematic illustrations of individual ribbon synapses (sizes and numbers not to scale). In the normal IHC synapse (left), the AZ is occupied by a synaptic ribbon (red) tethered to the presynaptic membrane by Bassoon (dark blue) accompanied by ribbon-associated and cytosolic synaptic vesicles (light green). Presynaptic Ca^{2+} channels (dark green) are clustered in a row underneath the ribbon (Frank et al., 2010), and glutamate receptor clusters (blue) on the postsynaptic SGN boutons assume a ring-like shape (Meyer et al., 2009; Fig. 3D). Bassoon has an unknown tertiary structure with a central RIBEYE-binding site (tom Dieck et al., 2005) and two double zinc finger domains in the n-terminal region that target synaptic membranes (Dresbach et al., 2003). In Bsn mutant synapses, the ribbon can be present (middle) or absent (right), Ca^{2+} channels are reduced in number, and the clusters are disorganized, whereas glutamate receptor rings and SGN boutons appear to be mostly preserved. The separation between remaining Bsn ^{gt} ribbons and the presynaptic membrane is increased. Insets, deconvolved higher-magnification images of representative synapses from ***A***.

μM) was added to block voltage-gated Na$^+$ channels. To depolarize presynaptic IHCs, 40 mM NaCl in the extracellular solution was replaced with equimolar KCl. Recordings were done at room temperature (21–23°C). After low-pass filtering at 10 kHz, EPSCs were detected and analyzed using Mini Analysis software (Synaptosoft). To classify the mode of EPSCs (i.e., monophasic or multiphasic), we followed the method standardized in a previous study (Grant et al., 2010).

Extracellular recordings from single SGN. For evaluation of the impact of bassoon disruption on sound encoding, we performed extracellular recordings from SGN as described previously (Taberner and Liberman, 2005; Strenzke et al., 2009). In brief, mice 5–11 weeks of age ($n = 12$ for Bsn^{gt}, $n = 10$ for WT$_{gt}$, $n = 11$ for Bsn$^{\Delta Ex4/5}$, $n = 2$ for Hz$_{\Delta Ex4/5}$, and $n = 13$ for WT$_{\Delta Ex4/5}$) were anesthetized by intraperitoneal injection of urethane (1.32 mg/kg), xylazine (5 mg/kg), and buprenorphine (0.1 mg/kg). An occipital approach with partial removal of the cerebellum was taken to advance a glass microelectrode during noise burst stimulation, aiming at identifying SGNs near the auditory nerve's entry zone into the cochlear nucleus and avoiding the posterior region of the anteroventral cochlear nucleus, where mainly spherical bushy cells are located. SGNs were distinguished from primary cochlear nucleus units based on the electrode position (electrode aiming at interior auditory canal, > 1 mm below the surface of cochlear nucleus) and their primary-like response characteristics to 200 suprathreshold 50 ms tone bursts presented at the characteristic frequency of the SGN, 30 dB above threshold. A coefficient of variation of interspike intervals of adapted responses > 0.5 confirmed

the irregular firing pattern observed in SGNs. The mean first spike latency did not allow for a clear separation between SGNs and anteroventral cochlear nucleus units firing at low rates. Erroneous unit type classification was more likely when spike rates were low, yielding less clear response patterns.

For each sound responsive unit, we first determined the spontaneous rate in a 10 s interval and if it was <10 or 2 Hz, an additional 10 or 20 s recording interval was added, respectively. We also determined the tuning curve by varying the frequency and intensity of 15 ms tone bursts using an automatically adapting procedure. For each frequency/intensity combination, we used a sequential probability test (Wald, 1947) with $p = 0.03$ to determine whether the resulting spike rate was equal to the spontaneous rate or to the threshold rate (the criterion being SR + 20 Hz) or if the measurement had to be repeated to reach statistical significance. The initial intensity step size of 16 dB was halved each time the threshold was crossed until a precision of 1 dB was reached. Similarly, we started with 1 octave frequency steps and halved the frequency steps for frequencies near the best frequency to determine the thresholds near the characteristic frequency (CF) with 1/32 octave precision. For tuning curves, spike detection was performed online based on a manually set trigger, whereas all other data were analyzed offline using a spike detection routine modified from the Wave_Clus routines (Quiroga et al., 2004). Compared with the method used by Buran et al. (2010) (described by Liberman, 1978), which compared spike rates directly during a 50 ms tone burst as being either higher or the same as those in the following 50

ms silent period, our tuning curve detection method yielded shorter recording times and better reproducibility of the data, albeit with a systematic slight threshold elevation for units with a large dynamic range.

Recording of auditory brainstem response and distortion product otoacoustic emissions. Animals were anesthetized intraperitoneally with a combination of ketamine (125 mg/kg) and xylazine (2.5 mg/kg) and the heart rate was monitored constantly to control the depth of anesthesia. The core temperature was maintained constant at 37°C using a rectal temperature-controlled heating blanket (Hugo Sachs Elektronik; Harvard Apparatus). For stimulus generation, presentation, and data acquisition we used the TDT System II (Tucker-Davis Technologies) run by BioSig32 software (TDT). Sound pressure levels are provided in dB SPL RMS (tonal stimuli) or dB SPL peak equivalent (PE, clicks) and were calibrated using a ¼″ microphone (D 4039, Brüel and Kjaer GmbH). Tone bursts (12 kHz, 10 ms plateau, 1 ms $\cos^2$ rise/fall) or clicks of 0.03 ms were presented at 20 Hz or 100 Hz in the free field ipsilaterally using a JBL 2402 speaker (JBL GmbH & Co.). The difference potential between vertex and mastoid subdermal needles was amplified (50,000 times), filtered (low pass: 4 kHz, high pass: 400 Hz) and sampled at a rate of 50 kHz for 20 ms, 2×2000 times to obtain two mean auditory brainstem responses (ABRs) for each sound intensity. Hearing threshold was determined with 10 dB precision as the lowest stimulus intensity that evoked a reproducible response waveform in both traces by visual inspection. For distortion product otoacoustic emissions, the ED1/EC1 speaker system (Tucker-Davis) was used to generate two primary tones (frequency ratio f2/f1: 1.2, intensity f2 = intensity f1 + 10 dB). Primary tones were coupled into the ear canal by a custom-made probe containing an MKE-2 microphone (Sennheiser) and adjusted to the desired sound intensities at the position of the ear drum as mimicked in a mouse ear coupler. The microphone signal was amplified and digitalized (DMX 6 Fire; Terratec) and analyzed by fast Fourier transformation (MATLAB; MathWorks).

Data analysis. Data analysis was performed using MATLAB, Igor Pro (Wavemetrics), and ImageJ software (http://rsb.info.nih.gov/ij/). For high magnification of individual synapses, the ImageJ plugin "deconvolution lab" was used, applying 10 iterations of the Richardson-Lucy algorithm. Figures were assembled for display in Adobe Photoshop and Adobe Illustrator software. Mean ΔC_m and Ca^{2+} current estimates are grand averages calculated from the mean estimates of individual IHCs. Means are expressed ± SEM. If applicable (i.e., normality of Jarque-Bera test and equal variances between [F test] the two samples), unpaired, two-tailed *t* tests were used for statistical comparisons between two sample groups. In all other cases, a Mann–Whitney–Wilcoxon test was used. Significance is shown as follows: *$p < 0.05$, **$p < 0.01$, ***$p < 0.001$, and n.s. (not significant).

Results

Defective ribbon anchorage in Bsn[gt] IHCs

For an assessment of the morphology of IHC afferent synapses in Bsn[gt] mutant mice, we used immunohistochemical colabeling of whole-mount preparations of the organ of Corti for the postsynaptic AMPA receptors GluA2, CtBP2/ribeye (labeling synaptic ribbons and sometimes nuclei), and presynaptic $Ca_v1.3$ Ca^{2+} channels (Fig. 1). Pairs of Bsn[gt] and WT[gt] samples were processed in parallel with identical immunolabeling and imaging protocols. Bsn[gt] ($n = 2264$ synapses in 199 IHCs) and WT[gt] ($n = 1682$ synapses in 148 IHCs) both had an average number of 11.4 GluA2-immunofluorescent spots per IHC in the tonotopic range of ~5–8 kHz, indicating preserved synaptic connectivity of IHCs with a normal number of afferent synapses. However, whereas in WT[gt] virtually all GluA2 spots (97.2%) had a juxtaposed synaptic ribbon (Fig. 1A, left), the majority of the mutant synapses were ribbonless (Fig. 1A, right), suggesting a defect of ribbon anchorage to the presynaptic membrane. On average, we found 43.6% ribbon-occupied synapses in Bsn[gt] IHCs (4–11 weeks of age with no clear age dependency), indicating a milder ribbon anchorage defect compared with Bsn[ΔEx4/5], in which an age-dependent decrease from ~47% at p11 (Fig. 5A,B) to 22% at p21 and 12% at
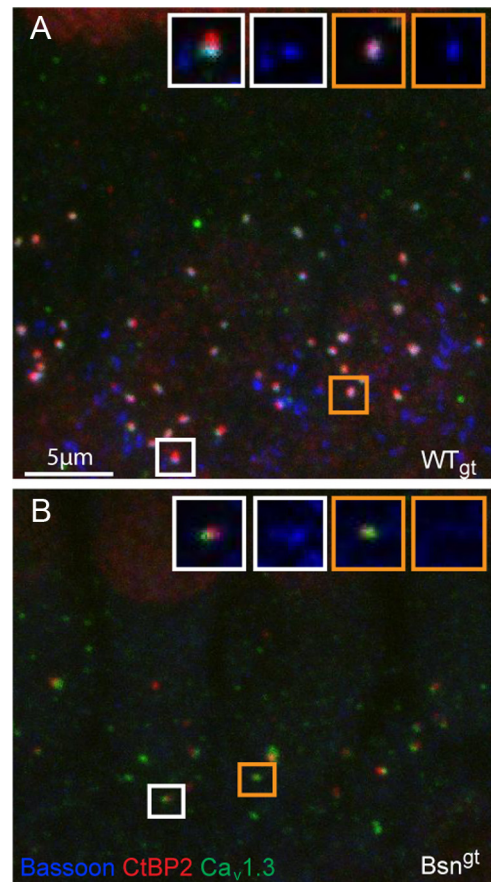

Figure 2. Residual expression of bassoon detected at a small subset of Bsn[gt] synapses. **A**, At synapses of WT[gt], IHCs immunolabeling of voltage-gated calcium channels ($Ca_v1.3$, green), synaptic ribbons (CtBP2, red), and bassoon (blue) resulted in a "sandwich-like" juxtaposition of fluorescent spots. Additional bassoon-positive, but CtBP2- and $Ca_v1.3$-negative, spots represent efferent synapses contacting SGN. Insets show two representative examples (white and golden frames, respectively) at higher magnification with all three channels (left) and bassoon channel only (right). Bassoon was clearly detectable at both synapses. **B**, At Bsn[gt] synapses, colocalization of bassoon with other synaptic markers rarely detectable by eye. Labeling is as in **A**. Insets demonstrate a weakly bassoon-positive synapse (white frames) and another synapse in which bassoon immunofluorescence did not exceed background (golden frames).

p70 was observed (Khimich et al., 2005). Ca^{2+} channels were clustered at WT[gt] and Bsn[gt] mutant synapses regardless of whether the ribbon was present.

We also analyzed Bsn[gt] mutant and WT[gt] ribbon-occupied synapses for the relative spatial organization of their presynaptic and postsynaptic densities and synaptic ribbons with nanometer precision. We measured the 3-dimensional center of mass distances between the CtBP2-, $Ca_v1.3$-, and GluA2-immunofluorescent spots in stacks of confocal images (Fig. 1B, $n = 99$ synapses for $Ca_v1.3$-CtBP2 distance in Bsn[gt] and $n = 250$ synapses for WT[gt], $p < 0.0001$; $n = 227$ synapses for GluA2-$Ca_v1.3$ distance in Bsn[gt] and $n = 263$ synapses in WT[gt], $p = 0.06$). The distance of CtBP2 spots to $Ca_v1.3$ and GluA2 spots in Bsn[gt] synapses was larger than at WT synapses, suggesting a looser ribbon anchorage to the presynaptic active zones, for which we had observed a trend based on a small sample of electron tomograms (Frank et al., 2010). In contrast, the distance between $Ca_v1.3$ and GluA2 spots was not significantly different between Bsn[gt] synapses and WT[gt] synapses, arguing for a predominantly presynaptic effect and against a more generalized disruption of the synaptic ultrastructure. Figure 1C schematically summarizes
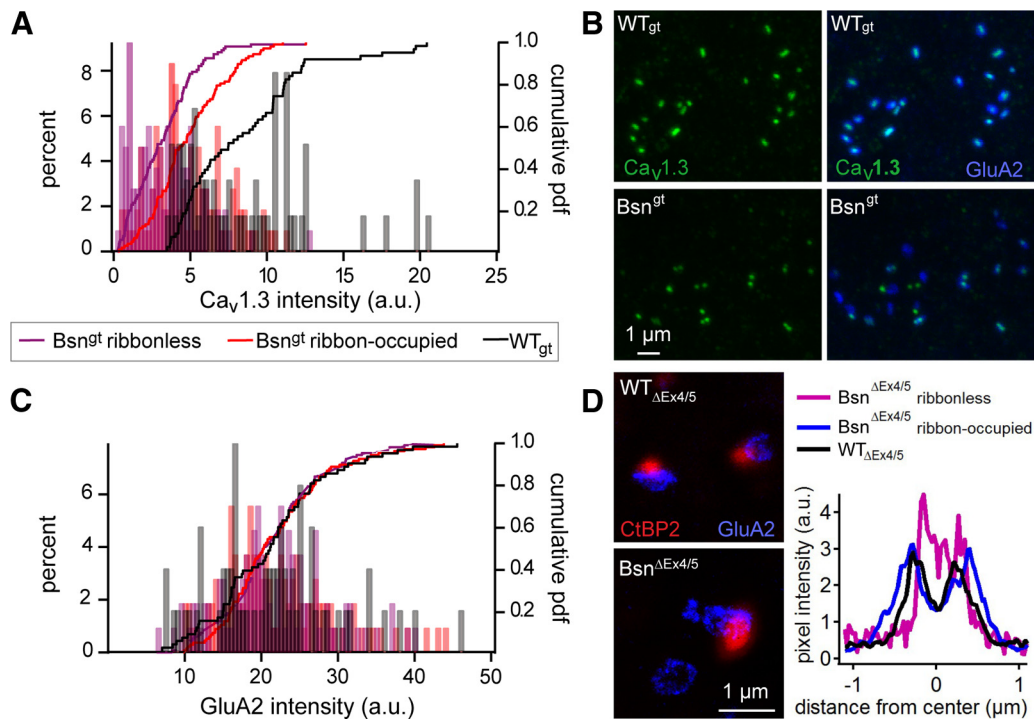
Figure 3. Altered presynaptic Ca^{2+} channel clusters and near normal postsynaptic AMPA receptor clusters at IHC synapses of Bsn mutants. *A*, Ca$_v$1.3 immunofluorescence in Bsn^{gt} IHCs (violet, $n = 108$ Bsn^{gt} ribbonless synapses; red, $n = 108$ Bsn^{gt} ribbon-occupied synapses) had reduced intensity compared with WT$_{gt}$ (black, $n = 105$ synapses). The analysis shown is derived from one representative pair of triple-stained samples as shown in Figure 1. Ribbon-occupied BSN^{gt} synapses harbor more Ca$_v$1.3 immunofluorescence than ribbonless synapses but less than WT$_{gt}$. *B*, Pair of double-stained preparations demonstrating the reduction in synaptic Cav1.3 (green), but not GluA2 receptor (blue), immunofluorescence. *C*, Distributions of GluA2 cluster immunofluorescence intensities of Bsn^{gt} and WT$_{gt}$ synapses overlapped (same preparation and color-codes as in *A*). *D*, Stimulated emission depletion microscopy demonstrating that ribbon-occupied and ribbonless synapses retained the ring-like morphology of GluA2/3 clusters (blue) in Bsn$^{\Delta Ex4/5}$ synapses, albeit with a slightly smaller diameter in the absence of a presynaptic ribbon (CtBP2, red, confocal mode).

the anatomy of WT (left), mutant ribbon-occupied (middle), and ribbonless synapses (right).

Leaky expression of bassoon in Bsn^{gt} IHCs may explain better ribbon anchorage than in Bsn$^{\Delta Ex4/5}$

The gene-trap strategy used to generate Bsn^{gt} mice interferes with transcription of the *bassoon* gene by insertion of a termination sequence between exons 1 and 2. Although there have been no reports of residual bassoon expression in Western blots or immunohistochemistry of brain tissue (Hallermann et al., 2010), a "leaky" transcription producing a small amount of whole-length mRNA could not be excluded. To understand the less severe defect of ribbon anchorage in IHCs of Bsn^{gt} compared with Bsn$^{\Delta Ex4/5}$, we studied the expression of bassoon on the mRNA and protein level in Bsn^{gt} organs of Corti. Using real-time PCR on cDNA, we found residual bassoon mRNA expression in Bsn^{gt} organs of Corti that amounted to 3% of WT levels (data not shown, $n = 6$ ears each). The expression level of mRNA coding for the 180 kDa protein fragment that remains expressed in Bsn$^{\Delta Ex4/5}$ mice was unchanged compared with the level of full-length mRNA in littermate controls (WT$_{\Delta Ex4/5}$, data not shown, $n = 2$ ears each). This fragment does not appear to be localized to synapses in immunohistochemistry of the brain (Altrock et al., 2003) and hair cells (Frank et al., 2010).

Consistent with its suspected role in ribbon anchorage, bassoon immunolabeling was detected at virtually all afferent WT IHC synapses that were colabeled by CtBP2 and Ca$_v$1.3 (Fig. 2A). Additional bassoon immunoreactivity was observed in the regions where synaptic terminals of lateral olivocochlear efferent fibers contacted the postsynaptic boutons of SGNs. In Bsn^{gt}, a

preparation double labeled for Ca$_v$1.3 and bassoon had indicated weak bassoon immunoreactivity overlapping with Ca$_v$1.3 clusters at < 5% of synapses (Frank et al., 2010). In additional triple-labeled preparations with inclusion of CtBP2 colabeling, bassoon was barely detectable. In that case, a visually detectable bassoon labeling was found at a single synapse (Fig. 2B, left) in a total of 72 IHCs.

In conclusion, the results of our RT-PCR experiments suggested that there was a small amount of leaky expression of bassoon in Bsn^{gt} IHCs that was, however, rarely detectable with immunohistochemistry. The presence of a few molecules of bassoon protein may support ribbon anchorage, albeit with looser coupling than at normal IHC ribbon synapses. This could explain the less severe ribbon anchorage phenotype in Bsn^{gt} compared with Bsn$^{\Delta Ex4/5}$ mutants.

Ca$_v$1.3 Ca^{2+} channels and AMPA receptors at ribbon-occupied and ribbonless synapses

We also investigated the effects of bassoon disruption on the presynaptic Ca$_v$1.3 Ca^{2+} channels and postsynaptic AMPA receptor clusters in Bsn^{gt} IHCs. We used immunohistochemistry for ribbons (CtBP2), Ca$_v$1.3 Ca^{2+} channels, and GluA2 (Fig. 1) for unequivocal definition of synaptic labeling and demonstrated a reduction of Ca$_v$1.3 immunofluorescence compared with WT$_{gt}$ that was more pronounced at ribbonless synapses based on a large number of ribbon-occupied and ribbonless Bsn^{gt} synapses (quantified in Fig. 3A). In another high-quality set of confocal images of IHCs from adult mice (p85) double stained for Ca$_v$1.3 and GluA2 (Fig. 3B), we analyzed WT$_{gt}$ ($n = 253$) and Bsn^{gt} ($n = 245$) synapses. We used GluA2 colabeling to differentiate synap-
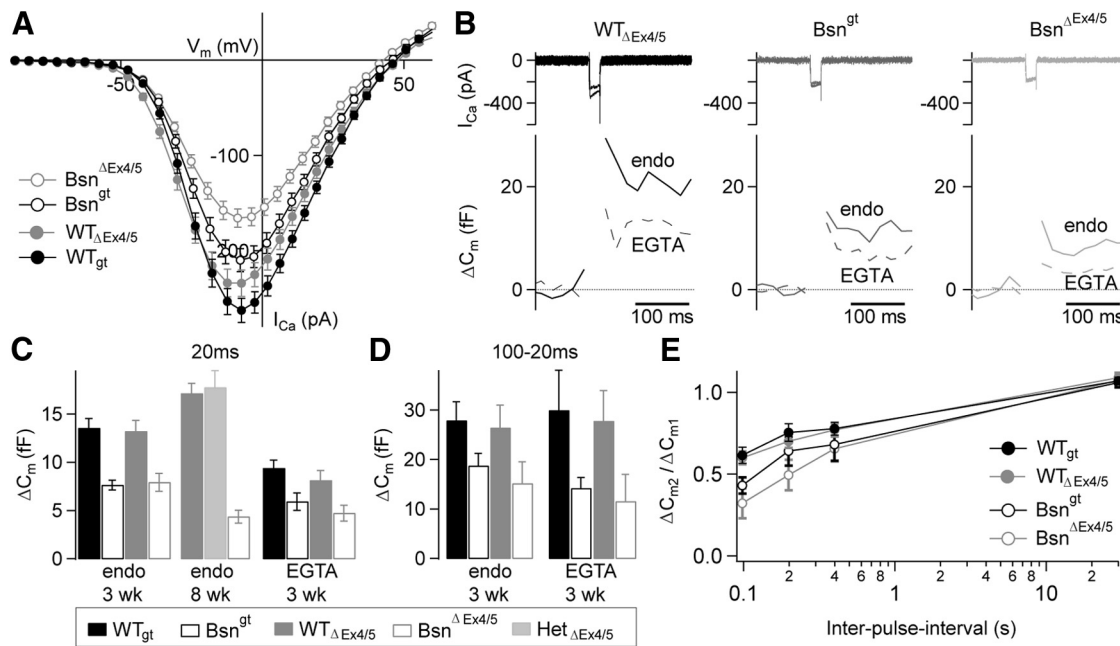
Figure 4. Patch-clamp analysis of IHC presynaptic function. *A*, Ca^{2+} current–voltage relationships from WT_{gt} (black closed circles, $n = 24$ IHCs), Bsn^{gt} (black open circles, $n = 26$), $WT_{\Delta Ex4/5}$ (gray closed circles, $n = 43$), and $Bsn^{\Delta Ex4/5}$ IHCs (gray open circles, $n = 46$). Peak Ca^{2+} currents were reduced to 71% of the value in WT littermates in $Bsn^{\Delta Ex4/5}$ ($p < 0.001$) and to 80% in Bsn^{gt} ($p < 0.01$), respectively. *B*, representative original capacitance recordings (bottom) from IHCs illustrating a comparable reduction in capacitance jumps after 20 ms depolarizations in Bsn mutants compared with WT IHC (mean reduction of 40% in $Bsn^{\Delta Ex4/5}$ and 44% in Bsn^{gt}). IHCs were depolarized to the membrane potential eliciting the maximum Ca^{2+} current (top). Replacing endogenous intracellular buffers ("endo" line) by 5 mM $[EGTA]_i$ (dashed lines) resulted in a comparable relative amount of suppression of exocytosis in all genotypes. *C*, RRP exocytosis (20 ms depolarizations) was reduced to a similar extent in both mutants (endogenous buffer, 3 wk; WT_{gt}: $n = 24$ IHCs, Bsn^{gt}: $n = 24$ IHCs, $WT_{\Delta Ex4/5}$: $n = 38$ IHCs, $Bsn^{\Delta Ex4/5}$ IHCs: $n = 37$ IHCs). Unaffected RRP exocytosis in heterozygous $Bsn^{\Delta Ex4/5}$ IHCs argues against a dominant-negative effect of the 180 kDa bassoon protein fragment on vesicle fusion (see text; endogenous buffer, 8 wk; $WT_{\Delta Ex4/5}$: $n = 7$ IHCs, $Hz_{\Delta Ex4/5}$: $n = 10$ IHCs, $Bsn^{\Delta Ex4/5}$ IHCs: $n = 9$ IHCs). Similar relative reduction of exocytosis across genotypes in the presence of 5 mM $[EGTA]_i$ suggests comparable coupling of vesicle fusion to presynaptic Ca^{2+} influx in both mutants (EGTA 3 wk; WT_{gt}: $n = 10$ IHCs, Bsn^{gt}: $n = 9$ IHCs, $WT_{\Delta Ex4/5}$: $n = 17$ IHCs, $Bsn^{\Delta Ex4/5}$ IHCs: $n = 16$ IHCs). *D*, Sustained exocytosis was more severely affected in $Bsn^{\Delta Ex4/5}$ than in Bsn^{gt} IHCs. Sustained exocytosis was assessed by (cell-wise) subtraction of capacitance jumps after 20 ms depolarizations from corresponding 100 ms counterparts (endogenous buffer, 3 wk; WT_{gt}: $n = 24$ IHCs, Bsn^{gt}: $n = 25$ IHCs, $WT_{\Delta Ex4/5}$: $n = 38$ IHCs, $Bsn^{\Delta Ex4/5}$ IHCs: $n = 36$ IHCs). $[EGTA]_i$ (5 mM) had comparable effects on both mutants ($p > 0.05$, EGTA 3 wk; WT_{gt}: $n = 8$ IHCs, Bsn^{gt}: $n = 9$ IHCs, $WT_{\Delta Ex4/5}$: $n = 11$ IHCs, $Bsn^{\Delta Ex4/5}$ IHCs: $n = 11$ IHCs). *E*, Paired pulse measurements showing that recovery from RRP depletion was slowed in both mutants, but to a lesser extent in Bsn^{gt} IHCs. Graph shows the grand average ratio of two capacitance jumps in response to two depolarization pulses of 20 ms duration at varying interpulse intervals (WT_{gt}: $n \geq 20$ IHCs, Bsn^{gt}: $n \geq 13$ IHCs $WT_{\Delta Ex4/5}$: $n \geq 23$ IHCs, $Bsn^{\Delta Ex4/5}$ IHCs: $n \geq 20$ IHCs, number provides minimum available for all intervals).

tic $Ca_v1.3$ clusters from extrasynaptic immunoreactivity and measured the extracellular background $Ca_v1.3$ immunofluorescence to subtract the nonspecific signal within each image. We found a tendency for a greater proportion of extrasynaptic $Ca_v1.3$ immunofluorescence in IHCs lacking bassoon, estimated on average to be $33.8 \pm 8\%$ in WT_{gt} and $38.5 \pm 15\%$ in Bsn^{gt}; however, this did not reach significance. This is consistent with our previous conclusions from functional analysis in $Bsn^{\Delta Ex4/5}$ IHCs (Frank et al., 2010).

Whereas the $Ca_v1.3$ immunofluorescence spots were significantly less intense in Bsn^{gt} compared with those of WT_{gt}, the mean intensities of GluA2 spots were not significantly different between genotypes and the distributions were nearly indistinguishable regardless of the presence of a ribbon (Fig. 3B,C). In agreement with previous work (Meyer et al., 2009), we observed a ring-like GluA2 immunofluorescence in stimulated emission depletion images of WT synapses (Fig. 3D, upper left), which was in principle maintained at both ribbon-occupied and ribbonless synapses of $Bsn^{\Delta Ex4/5}$ mutant mice (Fig. 3D, lower left). However, quantitative analysis indicated a slightly smaller ring diameter of ribbonless mutant synapses compared with ribbon-occupied mutant synapses (Fig. 3D, right; distance between peaks of average line profiles 528 ± 31 nm vs 691 ± 60 nm; $p < 0.05$; $n = 10$, 9, and 27 for $WT_{\Delta Ex4/5}$, $Bsn^{\Delta Ex4/5}$ ribbon-occupied, and ribbonless mutant synapses, respectively). In summary, IHCs of Bsn mutants contained as many afferent synapses as their WT litter-

mates and appeared to exhibit a normal number of postsynaptic AMPA receptors, whereas a subtle change in the shape of the AMPA receptor cluster was found in ribbonless $Bsn^{\Delta Ex4/5}$ synapses. Synapses from both mutants held fewer Ca^{2+} channels than WT and BSN^{gt} ribbonless synapses had a lower Ca^{2+} channel complement than BSN^{gt} ribbon-occupied synapses.

Effects of bassoon disruption on synaptic function: *in vitro* analysis

We also compared Ca^{2+} currents and exocytosis in Bsn^{gt} and $Bsn^{\Delta Ex4/5}$ IHCs of 3- to 4-week-old mice (p22–p32) in perforated patch recordings to assess whether the larger fraction of ribbon-occupied synapses in Bsn^{gt} IHCs was associated with better presynaptic function than in $Bsn^{\Delta Ex4/5}$ IHCs. Indeed, we found the Ca^{2+} currents of Bsn^{gt} IHCs to be intermediate between WT and $Bsn^{\Delta Ex4/5}$ IHCs (Fig. 4A; $p < 0.01$ for comparison of Bsn^{gt} vs $Bsn^{\Delta Ex4/5}$, both $p < 0.01$ vs WT) without any obvious difference in voltage dependence. In both mutants, exocytosis, measured as membrane capacitance increments in response to 20 ms (primarily recruiting the RRP) or 100 ms long depolarizations (to assess sustained exocytosis), was significantly reduced ($p < 0.01$; Fig. 4B–D). There was no significant difference between the responses of the Bsn^{gt} and $Bsn^{\Delta Ex4/5}$ IHCs to 20 ms depolarizations, suggesting a similar reduction of RRP exocytosis despite the different fraction of ribbon-occupied synapses (Fig. 4C). However, sustained exocytosis (approximated as the difference between

ΔC_{m100} and ΔC_{m20}) was less affected in Bsn^{gt} IHCs (Fig. 4D, 67% of WT$_{gt}$) than in Bsn$^{\Delta Ex4/5}$ IHCs (56% of WT$_{\Delta Ex4/5}$). Direct comparison revealed significantly more sustained exocytosis in Bsn^{gt} than in Bsn$^{\Delta Ex4/5}$ IHCs ($p < 0.01$ for comparison of ΔC_{m100}-ΔC_{m20} between Bsn^{gt} and Bsn$^{\Delta Ex4/5}$, $p < 0.05$ for comparing just ΔC_{m100}).

We also compared IHCs of heterozygote mice (HZ$_{\Delta Ex4/5}$) with those of WT$_{\Delta Ex4/5}$ mice for their response to 20 ms depolarization and found no significant differences (Fig. 4C), suggesting that the Bsn$^{\Delta Ex4/5}$ allele does not cause a dominant-negative phenotype. Intracellular application of 5 mM EGTA in whole-cell recordings did not cause a stronger relative suppression of exocytosis in either Bsn mutant compared with perforated patch, suggesting an unaltered tight coupling between synaptic Ca^{2+} channels and release ready vesicles (Fig. 4B–D). Finally, we found by paired pulse stimulation (20 ms pulses separated by different intervals) in perforated patch experiments that recovery of exocytosis after RRP depletion in Bsn^{gt} IHCs was slower than in WT$_{gt}$ IHCs ($p < 0.01$ for 100 ms interval), but faster than in Bsn$^{\Delta Ex4/5}$ IHCs ($p < 0.05$, Fig. 4E). Recovery of exocytosis after 100 ms depolarization of Bsn^{gt} IHCs was not significantly different from WT$_{gt}$, although a trend toward slower recovery was apparent (data not shown). We conclude that bassoon disruption leads to reduced Ca^{2+} influx and hair cell exocytosis, which, except for RRP exocytosis, is less pronounced in Bsn^{gt} mice than in Bsn$^{\Delta Ex4/5}$ mice.

We also performed whole-cell recordings from postsynaptic afferent boutons of type I SGNs at postnatal days 9–11 (Figs. 5, 6). We chose the Bsn$^{\Delta Ex4/5}$ strain for these challenging experiments because of their stronger phenotype compared with BSN^{gt}. At this age, Bsn$^{\Delta Ex4/5}$ IHCs still have almost half as many synaptic ribbons associated with GluA2-positive clusters compared with WT$_{\Delta Ex4/5}$ (on average, 5.1 in Bsn$^{\Delta Ex4/5}$, $n = 53$ IHCs, 4 ears; 10.7 in WT$_{\Delta Ex4/5}$, $n = 44$ IHCs, 3 ears). In agreement with the impaired exocytosis and vesicle replenishment in IHCs of Bsn mutants, we found a reduced rate of EPSCs at rest (0.11 ± 0.03 Hz in Bsn$^{\Delta Ex4/5}$, $n = 7$ boutons; 0.79 ± 0.26 Hz in WT$_{\Delta Ex4/5}$, $n = 8$ boutons, $p < 0.05$) and during application of 40 mM K$^+$ (0.59 ± 0.34 Hz in Bsn$^{\Delta Ex4/5}$, $n = 5$ boutons; 10.9 ± 3.70 Hz in WT$_{\Delta Ex4/5}$, $n = 5$ boutons, $p < 0.05$, Fig. 5C,D). EPSCs of WT$_{\Delta Ex4/5}$ and Bsn$^{\Delta Ex4/5}$ SGNs were variable in size and shape (Fig. 5C,E), as described previously in the rat and interpreted as MQR (Glowatzki and Fuchs, 2002). Every bouton of Bsn$^{\Delta Ex4/5}$ SGNs, like those of WT$\Delta_{Ex4/5}$, showed both small EPSCs with smooth rise and fall (monophasic) as well as larger EPSCs with more complex waveform (Fig. 5F, multiphasic). No segregation into different groups of SGNs (e.g., ribbon-occupied vs ribbon-less) was observed, but this analysis was hindered by the paucity
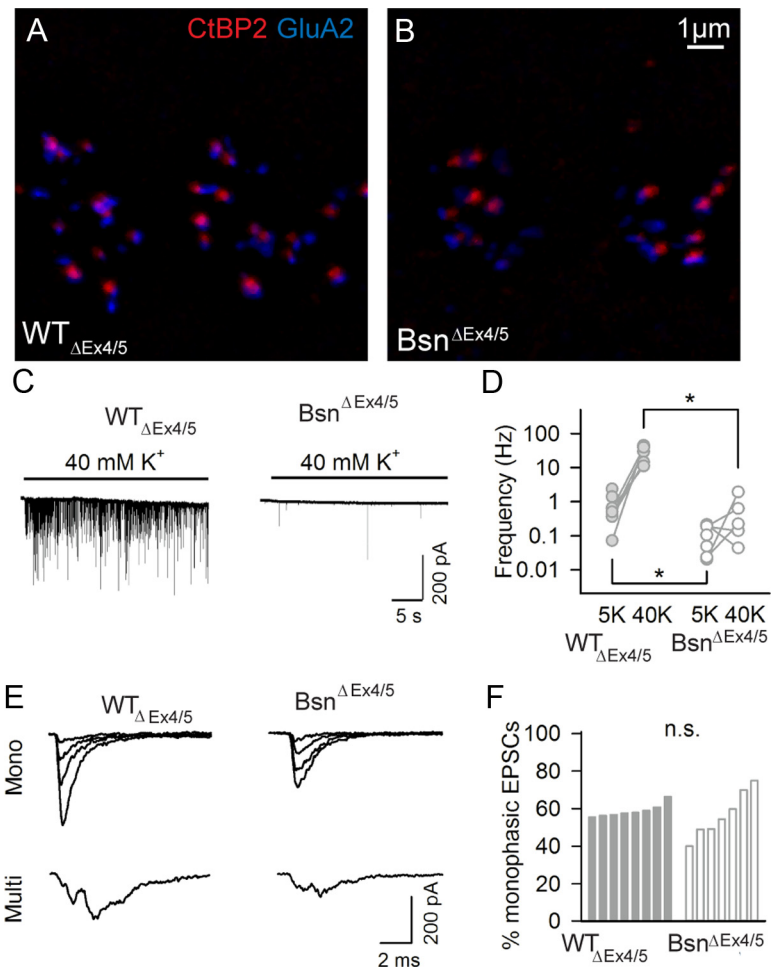

Figure 5. Patch-clamp recordings from postsynaptic SGN boutons of Bsn$^{\Delta Ex4/5}$ mutants. **A**, **B**, Synaptic regions of IHCs of p11 WT$_{\Delta Ex4/5}$ (**A**) and Bsn$^{\Delta Ex4/5}$ (**B**) mice, double-stained for GluA2 (blue) and CtBP2 (red), illustrating a relatively high ribbon occupancy in immature mutant IHC. **C**, Sample recordings of EPSCs from postsynaptic boutons of type I SGNs in WT$_{\Delta Ex4/5}$ (left) and Bsn$^{\Delta Ex4/5}$ (right). **D**, Frequency of EPSCs at rest (in artificial perilymph containing 5 mM K$^+$) and during IHC stimulation by application of artificial perilymph containing 40 mM K$^+$ for WT$_{\Delta Ex4/5}$ (filled circles) and Bsn$^{\Delta Ex4/5}$ (open circles). **E**, Sample traces of EPSCs in a millisecond scale to demonstrate their kinetics. Both monophasic and multiphasic EPSCs from WT$_{\Delta Ex4/5}$ and Bsn$^{\Delta Ex4/5}$ boutons are shown. **F**, Percentage of monophasic EPSCs derived from individual afferents of WT$_{\Delta Ex4/5}$ and Bsn$^{\Delta Ex4/5}$ SGN, respectively.

of events. The amplitudes of both monophasic EPSCs (81 ± 10 pA in Bsn$^{\Delta Ex4/5}$, $n = 7$ SGN; 142 ± 22 pA in WT$_{\Delta Ex4/5}$, $n = 8$ SGN, $p < 0.05$, Fig. 6A1,B) and multiphasic EPSCs (66 ± 11 pA in Bsn$^{\Delta Ex4/5}$; 105 ± 14 pA in WT$_{\Delta Ex4/5}$, $p < 0.05$, Fig. 6A2,B), as well as the synaptic charge transfer of the entire EPSC population (117 ± 8 fC in Bsn$^{\Delta Ex4/5}$; 191 ± 27 fC in WT$_{\Delta Ex4/5}$, $p < 0.05$, Fig. 6C,D), were on average nearly twofold smaller in Bsn$^{\Delta Ex4/5}$ SGNs. The kinetics of monophasic and multiphasic EPSCs was unaltered (Fig. 6E–H). Together with the barely changed postsynaptic GluA2 immunofluorescence, these results are compatible with a role of bassoon and/or the synaptic ribbon in promoting MQR.

Impaired sound coding in SGNs of Bassoon mice: *in vivo* analysis

To determine the functional consequences of the observed alterations in synaptic morphology and *in vitro* function, we analyzed *in vivo* sound encoding in SGNs in Bsn^{gt} and Bsn$^{\Delta Ex4/5}$ mice and their respective WT littermates. Previously, we observed in Bsn$^{\Delta Ex4/5}$ mice that firing rates were reduced in proportion with the reduction of presynaptic rate of exocytosis and RRP size (Buran et al., 2010; Frank et al., 2010). In the present study, we
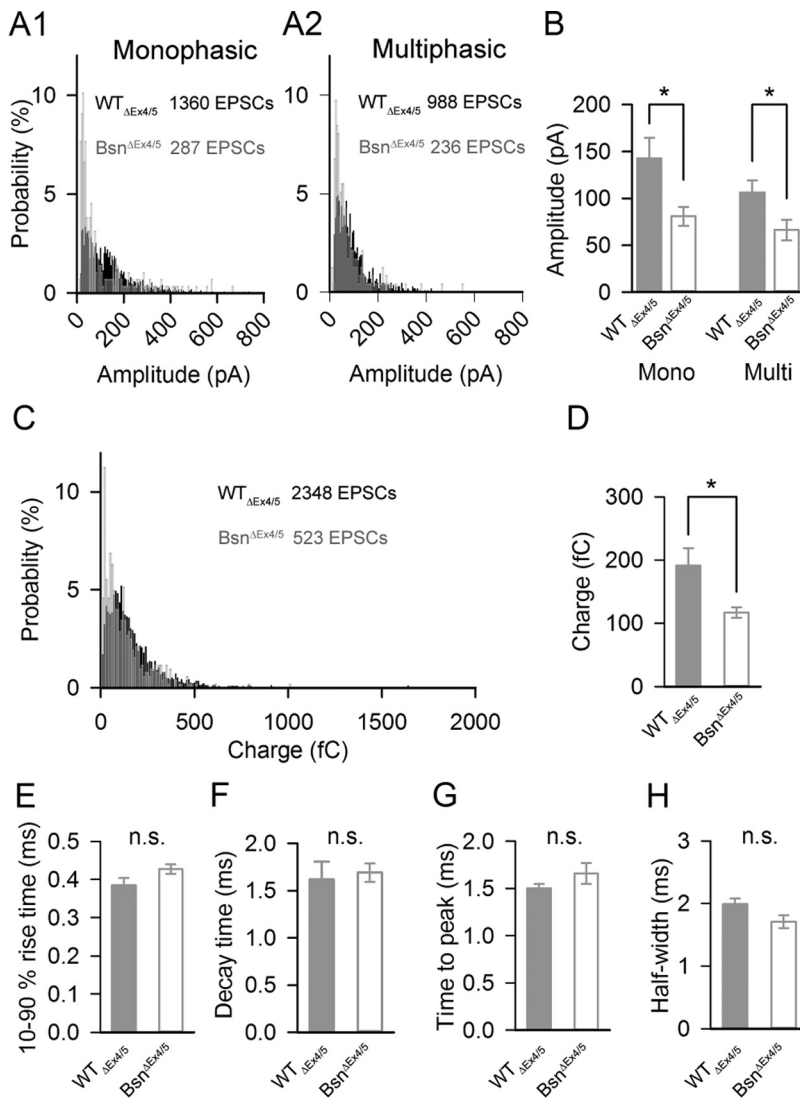
Figure 6. Analysis of EPSC size, kinetics, and waveforms. **A**, Pooled amplitude distribution of monophasic (**A1**) and multiphasic (**A2**) EPSCs and their grand averages (**B**). The distribution from Bsn $^{\Delta Ex4/5}$ (open bars) SGNs are shifted to smaller amplitudes compared with WT$_{\Delta Ex4/5}$ (gray bars), producing a significantly smaller mean amplitude, but the range of observed amplitudes was unchanged. **C, D**, Pooled charge transfer distributions (**C**) and their grand averages (**D**) of monophasic and multiphasic EPSCs derived from Bsn $^{\Delta Ex4/5}$ (gray) SGNs are reduced compared with WT$_{\Delta Ex4/5}$; however, the range was unchanged. **E–H**, The rise and decay times of monophasic EPSCs (**E,F**) and the time to peak and half-width of multiphasic EPSCs (**G,H**) from Bsn $^{\Delta Ex4/5}$ boutons were not significantly different from those of WT $^{\Delta Ex4/5}$ SGNs.

sought to test for better sound coding in a population of Bsn ^{gt} SGNs that could reflect encoding at ribbon-occupied synapses, which are more abundant in these mice. For a most reliable comparison, we studied the responses of SGNs from Bsn ^{gt}, Bsn $^{\Delta Ex4/5}$, HZ$_{\Delta Ex4/5}$, WT$_{\Delta Ex4/5}$, and WT$_{gt}$ to sound stimulation under identical experimental conditions. After isolating noise-stimulated single neuron firing activity near the internal auditory canal, we first characterized each unit by assessing their spontaneous rates (firing rates in the absence of sound stimuli), tuning curves, and responses to suprathreshold tone bursts at the CF of each unit and thereby identified SGNs. The hearing frequency range differed for the two mouse strains, presumably due to differences in the genetic background (Fig. 7A). No significant differences were observed for hearing thresholds (Fig. 7A), quality of tuning, or distortion product otoacoustic emissions (data not shown), arguing against a defect of cochlear amplification. Both mutants mostly lacked SGNs with high spontaneous rates (Fig. 7B). In

response to 50 ms tone burst stimulation at 30 dB above threshold at CF, SGNs showed a high instantaneous firing rate at stimulus onset that was followed by adaption (Fig. 7C), probably reflecting partial depletion of the RRP (Moser and Beutner, 2000; Goutman and Glowatzki, 2007; Buran et al., 2010) to a steady firing rate sustained throughout the stimulus duration. After the end of the stimulus, the firing rate dropped to almost zero, followed by a recovery of spontaneous activity if present. Bsn ^{gt} and Bsn $^{\Delta Ex4/5}$ SGNs showed virtually identical response patterns with similar adaptation time constants (Fig. 7D). We did not observe any segregation of groups of Bsn ^{gt} SGNs that would possibly indicate a difference between ribbon-occupied and ribbonless synapses. On average, evoked firing rates were significantly reduced by factors of 1.5 and 1.6, respectively, for Bsn ^{gt} and Bsn $^{\Delta Ex4/5}$ (Fig. 7D), and no significant differences between Bsn ^{gt} and Bsn $^{\Delta Ex4/5}$ SGNs were observed.

The spike rate reduction in both mutants was also obvious when examining average rates in responses to tone bursts of varying sound pressure levels at CF (Fig. 8A). These rate level functions had a shallower slope in both mutants and the dynamic range, the range of sound intensities over which 80% of the difference in rate between spontaneous and maximum occurs (Sachs et al., 1989), tended to be broader in the individual SGNs of both mutants (Fig. 8A–C). The increase in dynamic range was more pronounced in Bsn ^{gt} mice, but a tendency was also found in Bsn $^{\Delta Ex4/5}$ mice.

Finally, we studied recovery from forward masking by 100 ms tone bursts (Harris and Dallos, 1979; Fig. 8C). The masker elicits rapid adaptation that we attribute to depletion of the presynaptic RRP of vesicles and recovery, as revealed by the probe stimulus of identical intensity, that most likely reflects the replenishment of the RRP after the tone has ceased. According to the postulated roles of bassoon and/or the synaptic ribbon in vesicle replenishment (Frank et al., 2010; Hallermann et al., 2010) that was also indicated by our capacitance recordings (Fig. 4), we expected a slower recovery from masking that might be less pronounced in Bsn ^{gt} mice. However, we found similar time courses of recovery in Bsn ^{gt}, Bsn $^{\Delta Ex4/5}$, and WT littermate controls, which might indicate that vesicle replenishment of the smaller RRP at physiological temperature *in vivo* was sufficient.

Effect of bassoon disruption on auditory systems population responses

To assess the impact of spike rate reduction and spike asynchrony at the population level, we next analyzed ABR, of which wave I reflects the compound action potential of the SGNs (Melcher and Kiang, 1996; Melcher et al., 1996a, 1996b).
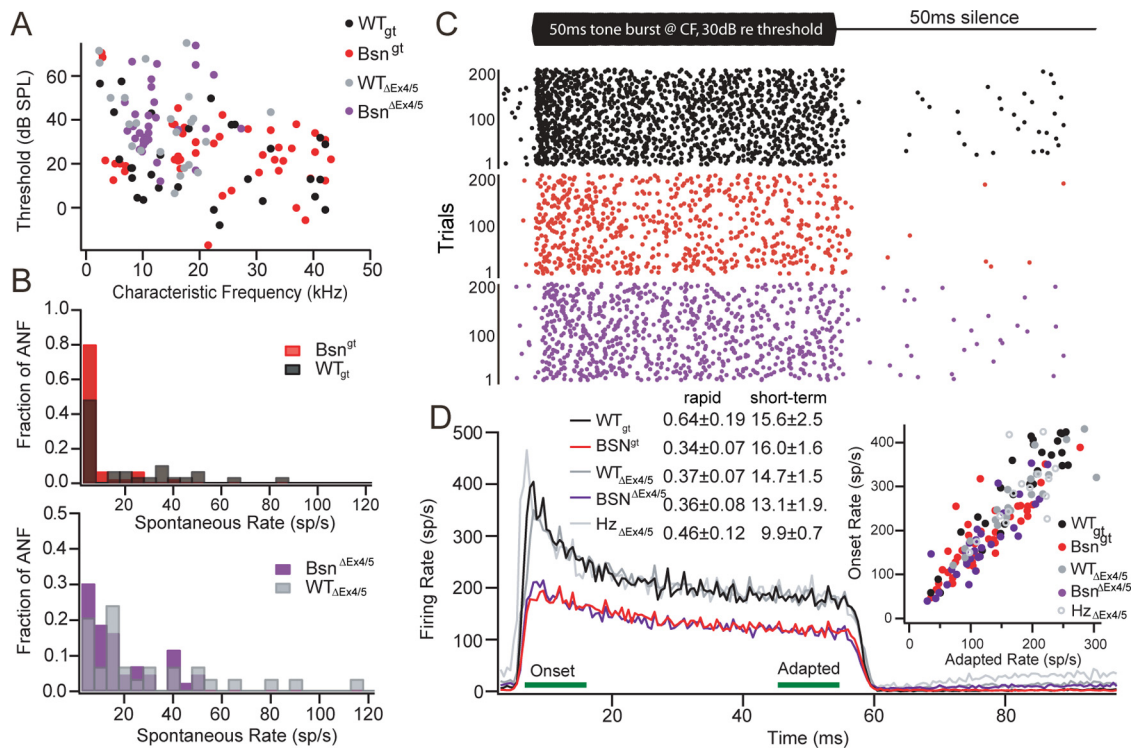
Figure 7. Basic characterizations of SGN responses *in vivo*. **A**, Best thresholds of individual SGNs of Bsn^{gt} (red, $n = 45$ SGNs), Bsn$^{\Delta Ex4/5}$ (purple, $n = 31$), and WT animals (black, $n = 29$ for WT$_{gt}$ and gray, $n = 23$ for WT$_{\Delta Ex4/5}$) as determined from the tuning curves tended to be elevated in both mutants compared with their respective WT controls ($p > 0.05$). **B**, Spontaneous spike rates are significantly reduced in SGNs from both mutant strains. **C**, Illustration of the firing pattern of representative WT$_{gt}$ (black, top), Bsn^{gt} (red, middle), and Bsn$^{\Delta Ex4/5}$ (violet, bottom) SGNs in response to 200 repetitions of a 50 ms tone burst presented at CF, 30 dB above thresholds. Each dot indicates a single action potential. **D**, Averaged poststimulus time histograms of SGN responses show a preserved activation pattern but reduced action potential firing rates in both mutants. Rapid and short-term adaptation time constants (double exponential fit for individual SGNs) were not significantly different. Inset: Onset and adapted rates (averaged in the 10 ms windows indicated by green bars) in all mutant SGNs were in the lower normal range. Responses from Hz$_{\Delta Ex4/5}$ SGNs (light gray line/gray open circles, $n = 16$) were indistinguishable from WT.

Spike rate and spike synchrony of activated SGN determine the latency, width, and amplitude of the compound action potential. The sound pressure levels evoking a reproducible threshold response were significantly elevated by approximately the same degree in Bsn^{gt} and Bsn$^{\Delta Ex4/5}$ mutants compared with the respective WT littermates (Fig. 9A). ABR thresholds of Bsn^{gt} mice were slightly elevated compared with those of Bsn$^{\Delta Ex4/5}$ mice, but because a similar increase was also found for WT$_{gt}$ mice compared with WT$_{\Delta Ex4/5}$ mice, this may have resulted from the different genetic backgrounds. The ABR waveforms evoked by suprathreshold click stimulation (80 dB peak equivalent) were comparable in Bsn^{gt} and Bsn$^{\Delta Ex4/5}$ mutants (Fig. 9B) and showed a massive reduction of wave I indicating a major reduction of synchronized activation of the SGNs, which is consistent with our results from single SGN recordings. A small potential preceding ABR wave I (probably representing the summating potential that primarily reflects the hair cell receptor potential) was unaffected in both mutants. We observed reduced amplitudes and a slight delay in latencies of all waves at all stimulus intensities. However, the amplitudes of central auditory responses (II and higher) were better preserved, possibly reflecting some degree of compensation by convergence of SGNs onto the neurons of the cochlear nucleus and/or homeostatic plasticity in the auditory brainstem nuclei. ABRs from all genotypes showed a comparable amplitude reduction when the click stimulus rate was increased from 20 to 100 Hz (data not shown). In summary, no significant differences were detected between Bsn^{gt}

and Bsn$^{\Delta Ex4/5}$ mutants despite an approximate twofold difference in the number of anchored ribbons per IHC.

Discussion

Each individual IHC ribbon synapse can drive spiking of a SGN at an instantaneous rate of up to 1 kHz at sound onset and up to a few hundred Hertz during sustained sound stimulation. Moreover, spike timing displays submillisecond precision (Kiang et al., 1965; Geisler, 1998). The molecular mechanisms underlying such vivid, sustained, and precise transmitter release are not well understood. Here, we took advantage of two genetic manipulations that disrupt bassoon, a key scaffold protein at the IHC active zone, to different extents. We propose that weak residual presence of bassoon at active zones of IHCs in Bsn^{gt} mice enabled better, but still disturbed, ribbon anchorage and maintained some aspects of synapse function beyond what we found in Bsn$^{\Delta Ex4/5}$ mice, which express only a nonfunctional bassoon fragment. However, other measures of synaptic function, in particular synaptic sound encoding in SGNs, were affected to the same extent. We did not observe a subpopulation of SGNs with WT-like firing rates, which would be expected if the ribbon-occupied synapses of mature Bsn^{gt} (44%) or Bsn$^{\Delta Ex4/5}$ (12%) mice were fully functional. Possible explanations include an impaired function of these synaptic ribbons due to looser anchorage or a ribbon-independent effect of the bassoon disruption on synaptic function.
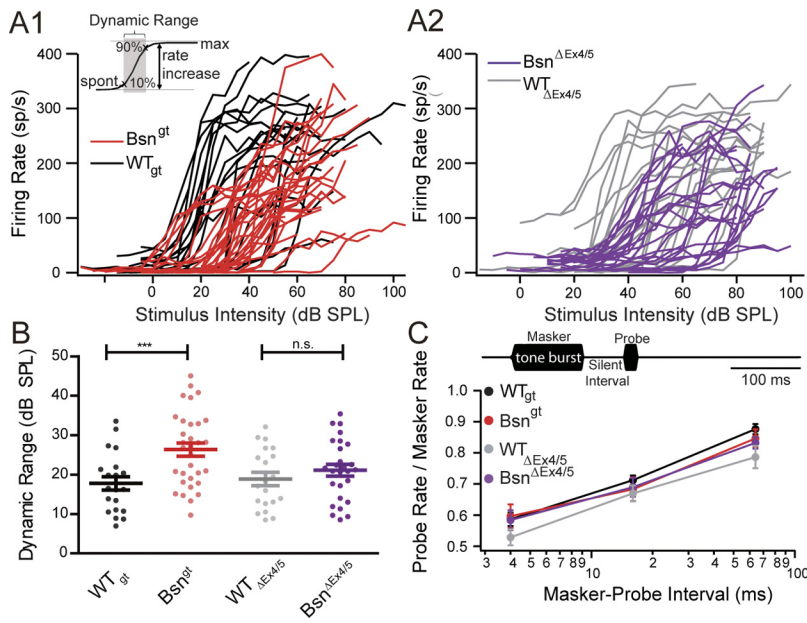
Figure 8. SGN responses *in vivo*: dynamic range and recovery from forward masking. **A1, A2,** Quantification of the overall spike rate in response to tone bursts presented at CF at varying sound intensities again demonstrate reduced spontaneous and sound-evoked spiking activity in Bsn ^{gt} (red, $n = 32$) SGNs compared with WT$_{gt}$ (black, $n = 20$) and in Bsn $^{\Delta Ex4/5}$ (violet, $n = 27$) compared with WT$_{\Delta Ex4/5}$ (gray, $n = 20$). Thresholds were not significantly different. Inset: Dynamic range is defined as the range of sound pressure levels in which the rate–intensity function exhibits a rate increase between 10% and 90% of the difference between spontaneous and maximal rate. **B,** Dynamic ranges of Bsn mutant SGNs were broader compared with WT (significant for Bsn ^{gt}). **C,** Top, illustration of the stimulus paradigm for forward masking experiment: 100 ms masker tone burst and a 15 ms probe tone burst are separated by a silent interval of varying duration. Both tone bursts are presented at CF, 30 dB above threshold. The duration of a complete cycle is 500 ms. Bottom, firing rates in response to the 15 ms probe stimulus presented as the fraction firing rate in the first 15 ms of the masker response indicate that the time course of recovery from forward masking was similar in all genotypes ($n = 29$ for Bsn ^{gt}, $n = 16$ for WT$_{gt}$, $n = 17$ for Bsn $^{\Delta Ex4/5}$, $n = 12$ for WT$_{\Delta Ex4/5}$).
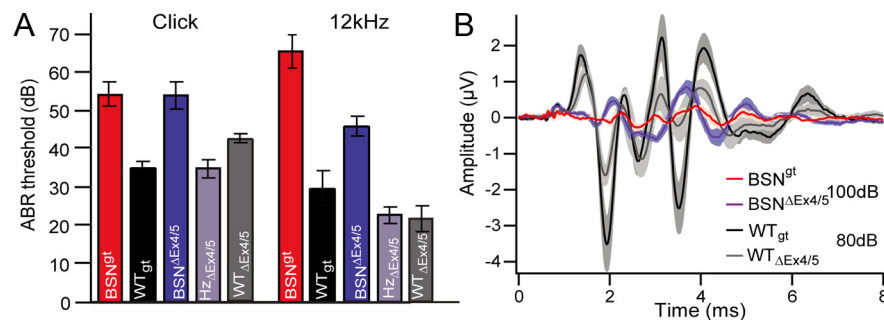

Figure 9. Auditory brainstem responses. **A,** ABR thresholds for click and 12 kHz tone burst stimuli are shifted to a comparable degree in Bsn ^{gt} and Bsn $^{\Delta Ex4/5}$ animals compared with their respective littermates, the latter displaying strain-dependent differences. **B,** Grand averages of ABR waves in response to 100 dB (mutants) or 80 dB (WT) click stimuli from Bsn ^{gt} (red, $n = 7$) and Bsn $^{\Delta Ex4/5}$ (purple, $n = 6$) mutants and WT$_{gt}$ (black, $n = 9$) and WT$_{\Delta Ex4/5}$ (gray, $n = 6$) controls, illustrating a pronounced reduction in amplitudes and minimal delay of all ABR peaks. ABR waveforms in Bsn $^{\Delta Ex4/5}$ heterozygous animals were equivalent to WT$_{\Delta Ex4/5}$ (data not shown).

Does the altered EPSC size distribution indicate a role of the ribbon in synchronizing MQR?

A role of the ribbon to promote the synchronous release of multiple vesicles (MQR) has been suggested since 1994, when Heidelberger et al. implied compound fusion to explain the instantaneous exocytosis of a retinal bipolar ribbon's complement of synaptic vesicles upon flash photolysis of caged Ca^{2+}. Nevertheless, proving this concept has remained challenging. For example, electron microscopical reports of large membranous organelles at the ribbon synapse (Lenzi et al., 2002; Matthews and Sterling, 2008) could either reflect compound exocytosis or bulk

endocytosis. The loss of synaptic ribbons from IHC synapses in Bsn $^{\Delta Ex4/5}$ mice (47% of WT$_{\Delta Ex4/5}$ at p11) offered direct access to address the role of the ribbon in MQR. Just as originally described for prehearing rats (Glowatzki and Fuchs, 2002), we found broad and positively skewed EPSC amplitude distributions in prehearing WT mice (Fig. 6; Pangršič et al., 2010). The EPSC amplitude distribution of Bsn $^{\Delta Ex4/5}$ boutons covered the normal range, but the mean amplitude was lower and fewer EPSCs exceeded 100 pA. The kinetics of monophasic and multiphasic EPSCs were unchanged. Therefore, the ribbon and/or functional bassoon seem to be supportive of, but not indispensable for, MQR. The smaller RRP in Bsn $^{\Delta Ex4/5}$ IHCs results in a longer and more variable first exocytosis latency (Khimich et al., 2005; Wittig and Parsons, 2008; Buran et al., 2010) and a smaller EPSC size, which is expected to further slow and time vary postsynaptic spike generation (Rutherford et al., 2012). Both mechanisms explain the longer and more variable SGN first spike latency *in vivo* in Bsn $^{\Delta Ex4/5}$ mice (Buran et al., 2010). Therefore, by promoting MQR, bassoon and/or the synaptic ribbon could contribute to fast and precise sound encoding at the first afferent synapse in the auditory pathway.

Bassoon is critical for anchoring synaptic ribbons in IHCs and auditory coding

The most prominent morphological change of photoreceptor and hair cell ribbon synapses in Bsn $^{\Delta Ex4/5}$ mutants is the loss of synaptic ribbons. Dick et al. (2003) argued that in photoreceptors, ribbons are absent from the start, because during synapse formation, the number of ribbon-occupied synapses is already low. In contrast, in IHCs, we found a gradual decrease of ribbon-occupied synapses from ~47% at the onset of hearing (Fig. 5) to 22% at 3 weeks of age (Frank et al., 2010) to 12% at 10 weeks of age (Khimich et al., 2005). Therefore, we consider it more likely that in Bsn $^{\Delta Ex4/5}$ IHCs, ribbons are initially present at most active zones, but cannot be stabilized there in the absence of functional bassoon.

Bsn ^{gt} IHCs maintained a higher fraction of ribbons (44%) throughout their development. In these mutants, a transcription termination sequence (gene trap) was inserted between exons 1 and 2, strongly reducing bassoon expression such that no protein was detected in Western blots from the brain (Hallermann et al., 2010). The observation of weak bassoon immunofluorescence at few Bsn ^{gt} IHC synapses (Fig. 2) and the finding of bassoon mRNA in real-time PCR reflect leaky expression of a small amount of bassoon that supports the long-term anchorage of a

fraction of ribbons. Alternatively, the remaining 180 kDa protein fragments composed of the fused N- and C-terminal domains may exert a dominant-negative effect in Bsn$^{\Delta Ex4/5}$ mice, in which only the central exons 4 and 5 of the bassoon gene in (including the RIBEYE-binding site; tom Dieck et al., 2005) are deleted. However, this fragment does not seem to localize to synapses (Altrock et al., 2003; Frank et al., 2010), such that it presumably cannot assume an aberrant scaffolding function even if it was capable of interaction. Normal hair cell exocytosis (Fig. 4) and spontaneous and evoked SGN spike rates (Fig. 7) and near-normal ABRs (Fig. 9) in heterozygous animals further argue against a dominant-negative effect of the truncated protein in Bsn$^{\Delta Ex4/5}$.

Because ribbon-occupied synapses showed abnormal but stronger Ca$_V$1.3 immunofluorescence than ribbonless synapses in Bsn^{gt} (Fig. 3) and Bsn$^{\Delta Ex4/5}$ mice (Frank et al., 2010), the lesser reduction of whole-cell Ca^{2+} current than in Bsn$^{\Delta Ex4/5}$ IHCs is consistent with the higher fraction of ribbon-occupied synapses and/or residual bassoon expression. In both Bsn mutants, rapid exocytosis and evoked spike rates were approximately halved, with no relative changes in adaptation or recovery from adaptation. Computational modeling suggested that the prevailing change of IHC synapses in Bsn$^{\Delta Ex4/5}$ mice was a reduction in the number of functional release sites (Frank et al., 2010). The same appears to be true for the Bsn^{gt} mutant. In addition, we have now also observed broadened rate-intensity functions of SGNs in both Bsn mutants. This effect was more prominent for the Bsn^{gt} mutant and extended beyond the broadening expected from the lower spontaneous rate of the mutant SGNs. Possible mechanisms explaining this difference include disproportionate changes in the numbers of Ca^{2+} channels and vesicular docking sites and the mild impairment of vesicle recruitment. In both cases, the release rate may vary over a broader range of stimulation intensities.

Ribbon or no ribbon: is that the question?
Although the IHCs of both Bsn mutants differed in the fraction of ribbon-occupied synapses, Ca^{2+} current, sustained exocytosis, and vesicle replenishment *in vitro*, sound coding *in vivo* was equally impaired. It is unclear at present why vesicle replenishment in Bsn^{gt} IHCs was better preserved only *in vitro*. This may be partly explained by differences in the experimental conditions, which may have favored the detection of subtle differences in the *in vitro* experiments. Indeed, the recovery time constant that we observed *in vitro* (140 ms for the fast and largest component of recovery, Moser and Beutner, 2000) was much longer than *in vivo* (47 ms; Fig. 8). Preliminary forward-masking experiments at different body temperatures suggest a major contribution of the temperature difference between the *in vitro* (room temperature) and *in vivo* (35°C) experiments, whereas we have no indication of age-dependent changes in RRP recovery. In addition, spontaneous synaptic calcium influx is mostly abolished at a holding potential of −87 mV *in vitro*, but may occur at the higher resting potential *in vivo* and may enable calcium-dependent enhancement of vesicle replenishment to the synapse.

Because an explanation of why the larger fraction of ribbon-occupied synapses in Bsn^{gt} IHCs did not translate into a better preservation of all aspects of synaptic function, we favor the hypothesis that those remaining ribbons were not fully functional. Alternatively, the sound-coding phenotype of Bsn mutants could be due to a direct effect of bassoon disruption and may be unrelated to the presence or absence of the ribbon. The lack of binding of bassoon to Ca$_V$1.3 Ca^{2+} channels (Frank et al., 2010) and the

mild (Hallermann et al., 2010) or absent (Mukherjee et al., 2010) alteration of presynaptic function by bassoon disruption at non-ribbon type active zones make this scenario less likely. In contrast, our result of a larger center of mass distance between ribbons and Ca$_V$1.3 or AMPA receptor clusters at ribbon-occupied synapses supports the notion of a looser anchorage at ribbon-occupied synapses in Bsn^{gt} IHCs. Such an increased distance to the active zone could impair a putative function of the ribbon in promoting a large number of synaptic Ca^{2+} channels and docking sites and in facilitating vesicle replenishment. This could come about by the reduced effect of ribbon-associated proteins with functions in scaffolding or regulation of docking and priming. Future experiments using photoablation of the remaining ribbons in Bsn^{gt} IHCs could help to distinguish these possible scenarios. However, the low number of ribbon-occupied synapses (on average, 4.6), the low RRP size (∼7.6 fF), and the requirement for a ruptured patch configuration (where rundown of presynaptic function is more prominent (Parsons et al., 1994; Moser and Beutner, 2000; Nouvian et al., 2011) make these experiments very challenging. Nevertheless, the advent of combinatorial approaches offers a fair chance to eventually clarify the roles of this enigmatic synaptic nanomachine.

References

Altrock WD, tom Dieck S, Sokolov M, Meyer AC, Sigler A, Brakebusch C, Fässler R, Richter K, Boeckers TM, Potschka H, Brandt C, Löscher W, Grimberg D, Dresbach T, Hempelmann A, Hassan H, Balschun D, Frey JU, Brandstätter JH, Garner CC, et al. (2003) Functional inactivation of a fraction of excitatory synapses in mice deficient for the active zone protein bassoon. Neuron 37:787–800. CrossRef Medline

Buran BN, Strenzke N, Neef A, Gundelfinger ED, Moser T, Liberman MC (2010) Onset coding is degraded in auditory nerve fibers from mutant mice lacking synaptic ribbons. J Neurosci 30:7587–7597. CrossRef Medline

Dick O, tom Dieck S, Altrock WD, Ammermüller J, Weiler R, Garner CC, Gundelfinger ED, Brandstätter JH (2003) The presynaptic active zone protein bassoon is essential for photoreceptor ribbon synapse formation in the retina. Neuron 37:775–786. CrossRef Medline

tom Dieck S, Brandstätter JH (2006) Ribbon synapses of the retina. Cell Tissue Res 326:339–346. CrossRef Medline

Dresbach T, Hempelmann A, Spilker C, tom Dieck S, Altrock WD, Zuschratter W, Garner CC, Gundelfinger ED (2003) Functional regions of the presynaptic cytomatrix protein bassoon: significance for synaptic targeting and cytomatrix anchoring. Mol Cell Neurosci 23:279–291. CrossRef Medline

Edmonds BW, Gregory FD, Schweizer FE (2004) Evidence that fast exocytosis can be predominantly mediated by vesicles not docked at active zones in frog saccular hair cells. J Physiol 560:439–450. CrossRef Medline

Emran F, Rihel J, Adolph AR, Dowling JE (2010) Zebrafish larvae lose vision at night. Proc Natl Acad Sci U S A 107:6034–6039. CrossRef Medline

Frank T, Rutherford MA, Strenzke N, Neef A, Pangršič T, Khimich D, Fejtova A, Gundelfinger ED, Liberman MC, Harke B, Bryan KE, Lee A, Egner A, Riedel D, Moser T (2010) Bassoon and the synaptic ribbon organize Ca2+ channels and vesicles to add release sites and promote refilling. Neuron 68:724–738. CrossRef Medline

Fuchs PA (2005) Time and intensity coding at the hair cell's ribbon synapse. J Physiol 566:7–12. CrossRef Medline

Geisler CD (1998) From sound to synapse. New York: Oxford UP.

Glowatzki E, Fuchs PA (2002) Transmitter release at the hair cell ribbon synapse. Nat Neurosci 5:147–154. CrossRef Medline

Goodman MB, Lockery SR (2000) Pressure polishing: a method for reshaping patch pipettes during fire polishing. J Neurosci Methods 100: 13–15. CrossRef Medline

Goutman JD, Glowatzki E (2007) Time course and calcium dependence of transmitter release at a single ribbon synapse. Proc Natl Acad Sci U S A 104:16341–16346. CrossRef Medline

Grant L, Yi E, Glowatzki (2010) Two modes of release shape the postsynaptic response at the inner hair cell ribbon synapse. J Neurosci 30:4210–4220. CrossRef Medline

Graydon CW, Cho S, Li GL, Kachar B, von Gersdorff H (2011) Sharp Ca2+ Nanodomains beneath the ribbon promote highly synchronous multivesicular release at hair cell synapses. J Neurosci 31:16637–16650. CrossRef Medline

Hallermann S, Fejtova A, Schmidt H, Weyhersmüller A, Silver RA, Gundelfinger ED, Eilers J (2010) Bassoon speeds vesicle reloading at a central excitatory synapse. Neuron 68:710–723. CrossRef Medline

Harris DM, Dallos P (1979) Forward masking of auditory nerve fiber responses. J Neurophysiol 42:1083–1107. Medline

Heidelberger R, Heinemann C, Neher E, Matthews G (1994) Calcium dependence of the rate of exocytosis in a synaptic terminal. Nature 371:513–515. CrossRef Medline

Hull C, Studholme K, Yazulla S, von Gersdorff H (2006) Diurnal changes in exocytosis and the number of synaptic ribbons at active zones of an ON-type bipolar cell terminal. J Neurophysiol 96:2025–2033. CrossRef Medline

Khimich D, Nouvian R, Pujol R, tom Dieck S, Egner A, Gundelfinger ED, Moser T (2005) Hair cell synaptic ribbons are essential for synchronous auditory signalling. Nature 434:889–894. CrossRef Medline

Kiang NYS, Watanabe T, Thomas EC, Clark LF (1965) Discharge patterns of single fibers in the cat's auditory nerve. Cambridge, MA: MIT.

Lenzi D, Crum J, Ellisman MH, Roberts WM (2002) Depolarization redistributes synaptic membrane and creates a gradient of vesicles on the synaptic body at a ribbon synapse. Neuron 36:649–659. CrossRef Medline

Li GL, Keen E, Andor-Ardó D, Hudspeth AJ, von Gersdorff H (2009) The unitary event underlying multiquantal EPSCs at a hair cell's ribbon synapse. J Neurosci 29:7558–7668. CrossRef Medline

Liberman MC (1978) Auditory-nerve response from cats raised in a low-noise chamber. J Acoust Soc Am 63:442–455. CrossRef Medline

LoGiudice L, Sterling P, Matthews G (2008) Mobility and turnover of vesicles at the synaptic ribbon. J Neurosci 28:3150–3158. CrossRef Medline

Matthews G, Fuchs P (2010) The diverse roles of ribbon synapses in sensory neurotransmission. Nat Rev Neurosci 11:812–822. CrossRef Medline

Matthews G, Sterling P (2008) Evidence that vesicles undergo compound fusion on the synaptic ribbon. J Neurosci 28:5403–5411. CrossRef Medline

Melcher JR, Kiang NY (1996) Generators of the brainstem auditory evoked potential in cat III: identified cell populations. Hear Res 93:52–71. CrossRef Medline

Melcher JR, Guinan JJ Jr, Knudson IM, Kiang NY (1996a) Generators of the brainstem auditory evoked potential in cat II. Correlating lesion sites with waveform changes. Hear Res 93:28–51. CrossRef Medline

Melcher JR, Knudson IM, Fullerton BC, Guinan JJ Jr, Norris BE, Kiang NY (1996b) Generators of the brainstem auditory evoked potential in cat. I. An experimental approach to their identification. Hear Res 93:1–27. CrossRef Medline

Meyer AC, Frank T, Khimich D, Hoch G, Riedel D, Chapochnikov NM, Yarin YM, Harke B, Hell SW, Egner A, Moser T (2009) Tuning of synapse number, structure and function in the cochlea. Nat Neurosci 12:444–453. CrossRef Medline

Moser T, Beutner D (2000) Kinetics of exocytosis and endocytosis at the cochlear inner hair cell afferent synapse of the mouse. Proc Natl Acad Sci U S A 97:883–888. CrossRef Medline

Mukherjee K, Yang X, Gerber SH, Kwon HB, Ho A, Castillo PE, Liu X, Südhof TC (2010) Piccolo and bassoon maintain synaptic vesicle clustering without directly participating in vesicle exocytosis. Proc Natl Acad Sci U S A 107:6504–6509. CrossRef Medline

Neef A, Khimich D, Pirih P, Riedel D, Wolf F, Moser T (2007) Probing the mechanism of exocytosis at the hair cell ribbon synapse. J Neurosci 27:12933–12944. CrossRef Medline

Nouvian R, Beutner D, Parsons TD, Moser T (2006) Structure and function of the hair cell ribbon synapse. J Membr Biol 209:153–165. CrossRef Medline

Nouvian R, Neef J, Bulankina AV, Reisinger E, Pangršič T, Frank T, Sikorra S, Brose N, Binz T, Moser T (2011) Exocytosis at the hair cell ribbon synapse apparently operates without neuronal SNARE proteins. Nat Neurosci 14:411–413. CrossRef Medline

Pangrsic T, Lasarow L, Reuter K, Takago H, Schwander M, Riedel D, Frank T, Tarantino LM, Bailey JS, Strenzke N, Brose N, Müller U, Reisinger E, Moser T (2010) Hearing requires otoferlin-dependent efficient replenishment of synaptic vesicles in hair cells. Nat Neurosci 13:869–876. CrossRef Medline

Parsons TD, Sterling P (2003) Synaptic ribbon. Conveyor belt or safety belt? Neuron 37:379–382. CrossRef Medline

Parsons TD, Lenzi D, Almers W, Roberts WM (1994) Calcium-triggered exocytosis and endocytosis in an isolated presynaptic cell: capacitance measurements in saccular hair cells. Neuron 13:875–883. CrossRef Medline

Quiroga RQ, Nadasdy Z, Ben-Shaul Y (2004) Unsupervised spike detection and sorting with wavelets and superparamagnetic clustering. Neural Comput 16:1661–1687. CrossRef Medline

Remé CE, Young RW (1977) The effects of hibernation on cone visual cells in the ground squirrel. Invest Ophthalmol Vis Sci 16:815–840. Medline

Rutherford MA, Pangršič T (2012) Molecular anatomy and physiology of exocytosis in sensory hair cells. Cell Calcium 52:327–337. CrossRef Medline

Rutherford MA, Chapochnikov NM, Moser T (2012) Spike encoding of neurotransmitter release timing by spiral ganglion neurons of the cochlea. J Neurosci 32:4773–4789. CrossRef Medline

Sachs MB, Winslow RL, Sokolowski BH (1989) A computational model for rate-level functions from cat auditory-nerve fibers. Hear Res 41:61–69. CrossRef Medline

Schmitz F (2009) The making of synaptic ribbons: how they are built and what they do. Neuroscientist 15:611–624. CrossRef Medline

Schwarz K, Natarajan S, Kassas N, Vitale N, Schmitz F (2011) The synaptic ribbon is a site of phosphatidic acid generation in ribbon synapses. J Neurosci 31:15996–16011. CrossRef Medline

Sheets L, Trapani JG, Mo W, Obholzer N, Nicolson T (2011) Ribeye is required for presynaptic CaV1.3a channel localization and afferent innervation of sensory hair cells. Development 138:1309–1319. CrossRef Medline

Singer JH, Lassová L, Vardi N, Diamond JS (2004) Coordinated multivesicular release at a mammalian ribbon synapse. Nat Neurosci 7:826–833. CrossRef Medline

Snellman J, Mehta B, Babai N, Bartoletti TM, Akmentin W, Francis A, Matthews G, Thoreson W, Zenisek D (2011) Acute destruction of the synaptic ribbon reveals a role for the ribbon in vesicle priming. Nat Neurosci 14:1135–1141. CrossRef Medline

Spiwoks-Becker I, Glas M, Lasarzik I, Vollrath L (2004) Mouse photoreceptor synaptic ribbons lose and regain material in response to illumination changes. Eur J Neurosci 19:1559–1571. CrossRef Medline

Strenzke N, Chanda S, Kopp-Scheinpflug C, Khimich D, Reim K, Bulankina AV, Neef A, Wolf F, Brose N, Xu-Friedman MA, Moser T (2009) Complexin-I is required for high-fidelity transmission at the endbulb of Held auditory synapse. J Neurosci 29:7991–8004. CrossRef Medline

Taberner AM, Liberman MC (2005) Response properties of single auditory nerve fibers in the mouse. J Neurophysiol 93:557–569. CrossRef Medline

tom Dieck S, Altrock WD, Kessels MM, Qualmann B, Regus H, Brauner D, Fejtová A, Bracko O, Gundelfinger ED, Brandstätter JH (2005) Molecular dissection of the photoreceptor ribbon synapse: physical interaction of Bassoon and RIBEYE is essential for the assembly of the ribbon complex. J Cell Biol 168:825–836. CrossRef Medline

von Gersdorff H, Vardi E, Matthews G, Sterling P (1996) Evidence that vesicles on the synaptic ribbon of retinal bipolar neurons can be rapidly released. Neuron 16:1221–1227. CrossRef Medline

Wald A (1947) Sequential analysis. New York: Wiley.

Wittig JH Jr, Parsons TD (2008) Synaptic ribbon enables temporal precision of hair cell afferent synapse by increasing the number of readily releasable vesicles: a modeling study. J Neurophysiol 100:1724–1739. CrossRef Medline